Check for updates

An insight into the outer- and inner-sphere electrochemistry of oxygenated single-walled carbon nanohorns (o-SWCNHs)†

Arvind S. Ambolikar, [ID] [ab] Saurav K. Guin [ID] *[a] and Suman Neogy[c]

The extremely large surface areas as well as connecting nanopores of single-walled carbon nanohorn (SWCNH) aggregates have been tested, for the first time to the best of our knowledge, as metal-free, stable and cheap electrocatalysts for heterogeneous electron transfer reactions involving inorganic redox couples, including f-block elements such as actinides. From systematic studies of heterogeneous electron transfer reactions, the electrochemically reversible outer-sphere heterogeneous surface insensitive electron transfer reaction involving $[Ru(NH_3)_6]^{3+}/[Ru(NH_3)_6]^{2+}$ and the electrochemically near-to-reversible inner-sphere heterogeneous surface sensitive electron transfer reaction involving $[Fe(CN)_6]^{3-}/[Fe(CN)_6]^{4-}$ on oxygenated SWCNHs (*i.e.*, o-SWCNHs) have been compared to heterogeneous electron transfer involving the quasi-reversible $[U^{(VI)}O_2(CO_3)_3]^{4-}/[U^{(V)}O_2(CO_3)_3]^{5-}$ redox reaction on o-SWCNHs. It was evident that the oxygen containing functional groups of o-SWCNH could catalyze the electron transfer process between uranium species in solution and the working electrode happened by following surface-sensitive inner-sphere electron transfer mechanism. Furthermore, the electrochemical stability, repeatability and reproducibility of the o-SWCNH modified glassy carbon electrode were found to be analytically acceptable for studying the electrochemistry of uranium in alkaline solutions with high ionic strength.

1. Introduction

Carbon nanomaterials have fascinated attention of researchers owing to their inimitable optical, electronic, thermal, mechanical, and chemical properties. Advances in fundamental and applied research on carbon nanomaterials have made them very competitive with metal or metal oxide nanomaterials by virtue of their diverse properties and low production costs, and the low toxicities of different carbon allotropes.[1] Single-walled carbon nanohorns (SWCNHs) were discovered by Iijima's group in 1999.[2–4] An individual SWCNH can be described as either conically rolled graphene or a cone-cap-ended single-walled carbon nanotube with a diameter of 2–4 nm and a length of 40–50 nm.[5,6] However, depending on the conditions of synthesis, SWCNHs usually form aggregates of different structures, such as dahlia-like, bud-like, seed-like, petal-dahlia-like, *etc.*, having average diameters in the range of 80–100 nm.[7–9] In contrast to

carbon nanotubes, highly pure SWCNHs can be produced economically on a large scale *via* thermal carbon sublimation, such as through arc discharge and laser ablation, without using any nano-metal catalysts.[4,10,11] However, progress relating to the research and development of SWCNHs is very slow in comparison to carbon nanotubes, mainly because of two factors. Firstly, the low symmetry of individual SWCNHs and their aggregates increases the difficulty of computationally modeling these structures for quantum mechanical simulations. Secondly, the formation of aggregates hinders in homogeneous dispersions of isolated SWCNHs and, hence, the functionalization and treatment of individual SWCNHs become difficult.[6] However, the exceptionally large surface areas, as well as favorable mass transport through the connecting nanopores of the SWCNH aggregates, promote the use of SWCNHs for various applications, such as in photoluminescence,[12,13] metal-assisted hydrogen storage,[14] electrochemical capacitors,[15–20] electrochemical sensors,[21–30] biosensors,[31–37] catalyst supports for fuel cells,[38–43] Li-ion batteries,[44] cathode materials[45] and electrolytes for dye-sensitized solar cells,[47] adsorbents,[48] nanomedicine and nanopharmacology,[49] *etc.*

Recently, SWCNHs have showed catalytic action in relation to I_3^-/I^- [46] and $[Co(bpy)_3]^{2+/3+}$ (bpy = 2,2′ bipyridine)[45] redox reactions, but their use for heterogeneous catalytic electron mediation is so far unexplored for other benchmark inorganic

[a] *Fuel Chemistry Division, Bhabha Atomic Research Centre, Trombay, Mumbai – 400085, India. E-mail: sauravkrguin@yahoo.co.in, skguin@barc.gov.in; Fax: +91-22-2550-5151; Tel: +91-22-2559-4591*

[b] *Homi Bhabha National Institute, Anushaktinagar, Mumbai – 400094, India*

[c] *Mechanical Metallurgy Division, Bhabha Atomic Research Centre, Trombay, Mumbai, 400085, India*

† Electronic supplementary information (ESI) available. See DOI: 10.1039/c9nj04467a

This journal is © The Royal Society of Chemistry and the Centre National de la Recherche Scientifique 2019

redox couples and industrially (nuclear energy sector) important f-block elements, such as actinides. In particular, the role of the surface bound oxygenated functional groups of o-SWCNH in electrocatalysis is unexplored to the best of our knowledge. Therefore, in this study, we examined redox reactions, such as an electrochemically reversible outer-sphere heterogeneous surface insensitive electron transfer reaction ($[Ru(NH_3)_6]^{3+}$/ $[Ru(NH_3)_6]^{2+}$ in 0.1 M KCl at pH 6.8)[50] and an electrochemically near-to-reversible inner-sphere heterogeneous surface sensitive electron transfer reaction ($[Fe(CN)_6]^{3-}$/$[Fe(CN)_6]^{4-}$ in 0.1 M KCl at pH 6.8),[50,51] to help gain an understanding of the role played by the surface-bound oxygenated functional groups of o-SWCNH in the electro-transfer reaction of the electrochemically quasi-reversible $[U^{(VI)}O_2(CO_3)_3]^{4-}$/$[U^{(V)}O_2(CO_3)_3]^{5-}$ redox couple in sat. Na_2CO_3 at pH 10.9.[52,53]

2. Experimental

2.1 Materials

Analytical grade potassium chloride (KCl), hexaammine-ruthenium(III) chloride ($[Ru(NH_3)_6]Cl_3$), potassium ferricyanide ($K_3[Fe(CN)_6]$), uranylnitrate hexahydrate ($UO_2(NO_3)_2 \cdot 6H_2O$), dimethylformamide (DMF) and sodium carbonate (Na_2CO_3) were used in this study. Ultrapure Milli-Q Millipore water (18.2 MΩ cm) was used to prepare all solutions. Partially oxidized SWCNHs (o-SWCNHs) were purchased from M/s Carbonium, Italy through M/s Global Nanotech, India. As per the information received from the supplier, the o-SWCNH aggregates were prepared *via* the induction heating of a graphite rod with a very intense, high frequency eddy current, followed by rapid condensation in the absence of any metal catalysts.[54] The oxygenated functional groups of the carbon nanomaterials were believed to serve dual roles in this study. The initial hypothesis was that a couple of oxygenated functional groups from the o-SWCNHs may serve as active centers for the electron transfer reactions and, on the other hand, a few may mediate electrons to uranium through pseudo-redox reactions. This hypothesis was initially tested through cyclic voltammetry experiments involving the U(VI)/U(V) redox reaction on o-SWCNHs and electrochemically reduced o-SWCNHs, which will be discussed below. Hence, all studies relating to the above-mentioned objectives were performed with commercially imported o-SWCNHs.

2.2 Instrumentation

The morphology of the o-SWCNHs was observed using a high-resolution CARL ZEISS LIBRA 200 FE transmission electron microscope (TEM) operated at 200 kV. The physico-chemical nature of the o-SWCNHs was studied using an Alpha table-top Fourier transform infrared (FTIR) spectrophotometer with a 4 cm^{-1} resolution over the wavenumber range of 500–4000 cm^{-1}, a Seki STR300 Raman spectrometer with a 532 nm DPSS laser excitation source, a Rigaku Smart Lab X-ray diffractometer (XRD) with a Cu K$_\alpha$ excitation source, and an X-ray photoelectron spectrometer (XPS) consisting of a Mg K$_\alpha$ (E = 1253.6 eV) X-ray (SPECS system) source and a PHOIBOS hemispherical channel

analyzer (HSA3500 DLD 150 R7 [HW Type 30:101] DLD). The electrochemical experiments were carried out at room temperature (T = 298 ± 1 K) using CHI-450B and Autolab-PGSTAT30 electrochemical workstations in a 10 mL electrochemical cell consisting of a working electrode (either GC or o-SWCNH modified GC (o-SWCNH/GC)), a platinum counter electrode and an Ag/AgCl (saturated (sat.) KCl) reference electrode. All the potentials reported in this manuscript are with reference to the Ag/AgCl (sat. KCl) electrode. The detailed operational parameters of the electrochemical experiments, such as cyclic voltammetry, cathodic square wave voltammetry and electrochemical impedance spectroscopy, are given in the respective places in the discussion.

2.3 Procedures

Before the electrochemical experiments, high purity nitrogen was purged into the electrolyte solution to remove dissolved oxygen. The GC electrode was polished using a slurry of alumina powder and washed thoroughly with water under ultrasonication. 5 μL of dispersed o-SWCNH in DMF (the concentration of o-SWCNH was 1 mg mL^{-1}) was drop-cast onto the GC electrode, which was dried under IR light.

3. Results and discussion

3.1 Morphology and crystallography of o-SWCNHs

A TEM image of o-SWCNHs shows the coexistence of bud-like and dahlia-like aggregates, as reported in other literature studies (Fig. 1[A]).[7,55,56] Variations in the pressure of the carrier gas in the synthesis chamber might be responsible for the mixed morphologies of the aggregates.[7] The mean lateral sizes of the bud-like and dahlia-like aggregates were calculated as 46.0 ± 16.6 nm (number = 29) and 79.5 ± 12.1 nm (number = 31), respectively, as shown in the histogram (Fig. S1, ESI†). The diameters of the bud-like and dahlia-like aggregates were found to be in the ranges of 15.0–83.6 nm and 55.0–102.5 nm, respectively. Fig. 1[B] shows the complete morphology of the dahlia-like aggregates of o-SWCNHs. Close inspection further reveals the very strong and robust coalescence of thin graphene sheets and o-SWCNHs inside each dahlia-like aggregate. There were many closed-end horn-like nanostructures near the peripheral surface of each dahlia-like aggregate and one of these is shown in Fig. 1[C]. The average length, base-width and tip-width of that specific nanohorn were calculated to be about 22 nm, 11.5 nm and 3.5 nm, respectively. The tubular structures of o-SWCNHs can be seen as near-to-parallel dark lines in a HR-TEM image of the dahlia-like aggregate (Fig. 1[D]).[4,57] The average separation distances between the walls of two adjacent tubes at the base and tip of the nanohorn were 0.382 nm and 0.361 nm, respectively. Since, the nanotubes in the aggregate form bundle-type structures due to strong van der Waals interactions, it could be understood that the o-SWCNHs at the horns strongly interacted with each other.

The XRD pattern of o-SWCNHs showed one broad diffraction peak centered at 2θ = 23.6°, with a broad peak at around
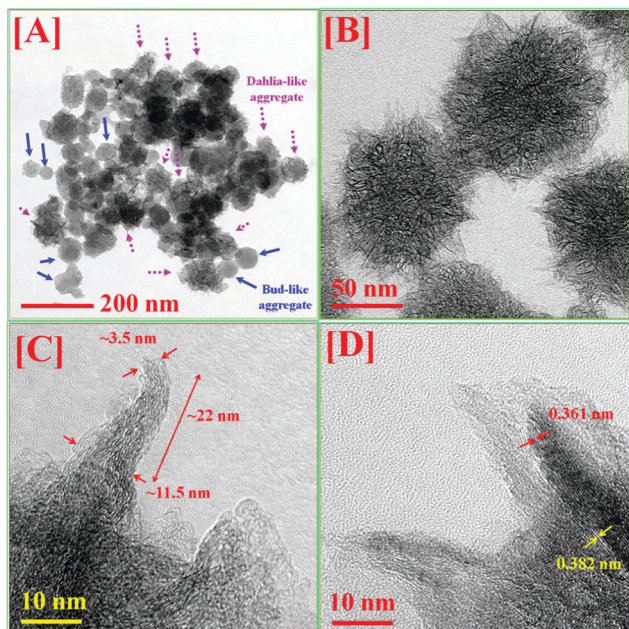
Fig. 1 [A] A TEM image of coexisting bud-like (as shown by the blue arrows) and dahlia-like (as shown by the pink broken arrows) aggregates of o-SWCNHs. [B] A magnified TEM image of dahlia-like aggregates of o-SWCNHs. [C and D] HR-TEM images of o-SWCNHs.

Fig. 2 [A] FTIR, [B] Raman, and high-resolution binding energy [C] C_{1s} and [D] O_{1s} XPS spectra of o-SWCNHs.

29.1° and a small peak at 43.4° (Fig. S2, ESI†). The first diffraction peak represents the Bragg reflection of (002) carbon planes having an average lattice spacing of about 0.376 nm, which is slightly wider than pristine graphite (0.335 nm).[57] On the other hand, the wide hump with a lattice spacing of 0.307 nm is a little more compact than pristine graphite. The small diffraction peak at 43.4° (with a lattice spacing of 0.208 nm) represents the (101) planes of the graphite-like structure.[57–59] Therefore, the morphological and crystallographic diversities of o-SWCNHs inspired the extension of our studies to their outer-sphere and inner-sphere electron transfer properties.

3.2 Chemical functionality of o-SWCNHs

Fig. 2[A] shows the FTIR spectrum of o-SWCNHs. Characteristic peaks are seen from (C–O)$_{in-plane\ bending}$ and (CH$_2$)$_{in-plane\ rocking}$ at 668 and 720 cm^{-1}; (O–H)$_{deformation}$, (C–O–C)$_{stretching}$, the stretching of ether or alkoxy linkages at 803, 872 and 1019 cm^{-1}; (C–O)$_{stretching}$ of aliphatic alcohols, saturated aliphatic esters, epoxy or phenol groups, and carboxyl groups at 1113, 1164, 1260 and 1384 cm^{-1}; (C–O–C)$_{stretching}$ of epoxy groups, (C=C)$_{stretching}$ of aromatic rings, (C=C)$_{stretching}$ of alkenes, (C=O)$_{stretching}$ of carbonyls, aldehydes and acids, (=C–H)$_{stretching}$ of aldehydes, (C–H)$_{stretching}$ of aliphatic and aromatic units, and (O–H)$_{stretching}$ of alcohols at 1459, 1558, 1653, 1743, 2852, 2922 and 2955, and 3416 cm^{-1}, respectively, confirming that o-SWCNHs possess several oxygenated functional groups along with the main graphene-type backbone.[60] Atmospheric CO_2 introduced a pair of IR peaks at 2344 and 2362 cm^{-1}.

The Raman spectrum of o-SWCNH (Fig. 2[B]) showed that a topological D-band at 1328 cm^{-1} was originated from the combination of 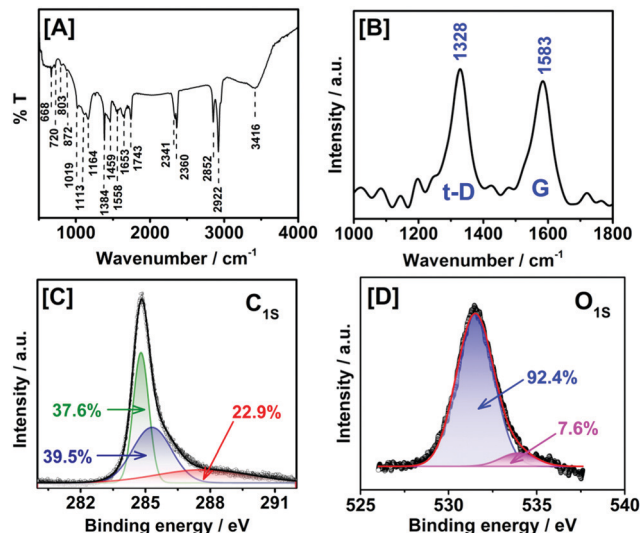the A_{1g} lattice vibration modes at the zone and the normal D-band excited near the edge of the o-SWCNHs. It differed by 30–50 cm^{-1} from the D-band activation at the edge of the graphene layer observable in the wavenumber range of 1365–1385 cm^{-1}. This is attributed to a lack of homogeneous distinction between the carbon atoms in o-SWCNHs due to the presence of many pentagonal topological defects in very close proximity to the carbon honeycombs.[61] The G-band observed at 1583 cm^{-1} was originated from the degenerate E_{2g} lattice vibration modes of the hexagonal carbon lattice. The intensity ratio of the topological D-band to the G-band was calculated as 1.04, which confirmed the presence of topological defects in the honeycomb base structure of o-SWCNH.

The XPS survey spectrum of o-SWCNHs is shown in Fig. S3 (ESI†). The peaks at 284.7 and 531.5 eV represent the C_{1s} and O_{1s} binding energies. Background features below 10% with respect to the C_{1s} intensity were neglected. The C/O ratio of o-SWCNHs was calculated to be 2.3 from the respective peak areas. Therefore, the topological defects in o-SWCNHs, as observed from the Raman spectrum, were mostly contributed by the pentagonal carbon structures in the carbon honeycomb lattice rather than the attached oxygenated functional groups. The high-resolution binding energy profile of the C_{1s} peak centered at 284.8 eV could be de-convoluted into three peaks centered at 284.7 eV (37.6%), 285.3 eV (39.5%) and 287.7 eV (22.9%) (Fig. 2[C]). On the other hand, the high-resolution binding energy profile of the O_{1s} peak centered at 531.5 eV could be de-convoluted into two peaks centered at 531.5 eV (92.4%) and 533.9 eV (7.6%) (Fig. 2[D]). It confirmed that the major constitutional components of the o-SWCNHs were sp^2 carbon atoms from the honeycomb backbone, sp^3 carbon atoms at the edges, and pentagonal defects and carbonyl (C=O) carbon atoms in acid, ketone and aldehyde functional groups.[62]

3.3 The electrochemical properties of o-SWCNHs

The electrochemical features of o-SWCNH/GCs in comparison to bare GC were studied *via* cyclic voltammetry in sat. Na_2CO_3

(pH 10.9) solution at a scan rate (ν) of 25 mV s^{-1} (Fig. 3[A]). o-SWCNH/GC showed a higher background current compared to bare GC. The anodic peak at about −0.388 V and the corresponding cathodic current over a wide potential range can be attributed to redox reactions representing the desorption of hydroxyl (–OH) groups in combination with the formation of carbonyl (C=O) and carboxyl (HO–C=O) functional groups, which have been evidenced to be electrochemically stable under the present voltammetric experimental conditions.[63–66] A cathodic current surge near −1.5 V was observed due to the evolution of molecular hydrogen on o-SWCNH/GC (eqn (1)):

$$2H_2O + 2e^- \rightarrow H_2 + 2OH^- \qquad (1)$$
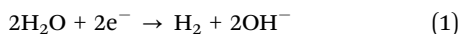
From preliminary inspections, it can be seen that the overpotential for hydrogen evolution in sat. Na$_2$CO$_3$ (pH 10.9) decreased by about 100 mV using o-SWCNH/GC compared to the GC electrode. The anodic peak current (I_p^a) of o-SWCNH/GC increased as ν increased over the range of 0.025–0.300 V s^{-1} (inset of Fig. 3[A]), and the slope of the straight line of a plot of $\ln(I_p^a)$ versus $\ln(\nu)$ was calculated as 0.81 (Fig. 3[B]). Here, we should declare that slopes of 1.0 and 0.5 in a plot of $\ln(I_p^a)$ versus $\ln(\nu)$ theoretically represent ideal surface-bound and diffusion-limited voltammetric events, respectively. Hence, we could conclude that the anodic peak at about −0.388 V originated from the desorption of hydroxyl (–OH) groups in combination with the formation of carbonyl (C=O) and carboxyl (HO–C=O) functional groups at the surface of o-SWCNHs.[63] However, the electrochemical stability of o-SWCNH/GC was found to be quite satisfactory for further explorations. For initial comparative trial experiments, electrochemically reduced o-SWCNH/GC was prepared via keeping an o-SWCNH/GC electrode in sat. Na$_2$CO$_3$ (pH 10.9) at −1.6 V for 240 s. From our previous research involving oxygenated carbon nanomaterials, this was believed to be satisfactory for this purpose.[52,60,67]

Fig. 4[A] shows CVs of 5 mM K$_3$[Fe(CN)$_6$] in 0.1 M KCl (pH 6.8) on GC and o-SWCNH/GC electrodes at ν = 25 mV s^{-1}. The cathodic (E_p^c) and anodic (E_p^a) peaks from the [Fe(CN)$_6$]$^{3-}$/[Fe(CN)$_6$]$^{4-}$ redox reaction on bare GC were observed at 0.227 and 0.298 V, respectively, resulting in a peak-to-peak separation (ΔE_p) of 71 mV. On the other hand, the E_p^c and E_p^a peaks from the same redox reaction on o-SWCNH/GC were observed at
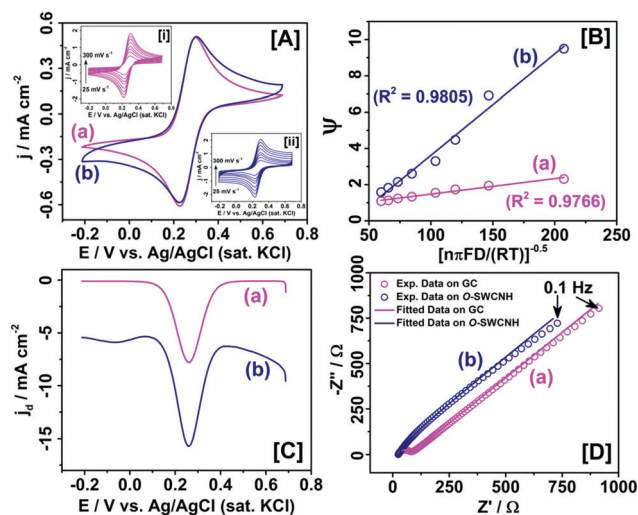
Fig. 4 [A] CVs of 5 mM K$_3$[Fe(CN)$_6$] in 0.1 M KCl (pH 6.8) on (a) GC and (b) o-SWCNH/GC electrodes at ν = 25 mV s^{-1}; inset: CVs from the same system on [i] GC and [ii] o-SWCNH/GC electrodes at ν = 25, 50, 75, 100, 150, 200, 250 and 300 mV s^{-1}. [B] Plots of Ψ versus $\dfrac{1}{\left[\dfrac{n\pi FD\nu}{RT}\right]^{\frac{1}{2}}}$ for the same reaction on (a) GC and (b) o-SWCNH/GC. [C] Difference current density (j_d) values from cathodic square wave voltammograms (cSWVs) for the reduction of [Fe(CN)$_6$]$^{3-}$ in 0.1 M KCl on (a) GC and (b) o-SWCNH/GC. The square wave pulse amplitude and frequency were 0.05 V and 50 Hz, respectively. [D] Nyquist plots of 5 mM K$_3$[Fe(CN)$_6$] in 0.1 M KCl (pH 6.8) on (a) GC and (b) o-SWCNH/GC electrodes. The potential was kept constant at 0.263 V with a sine potential perturbation with an amplitude of 5 mV over the frequency range of 1 × 10^5 to 1 × 10^{-1} Hz.

0.233 and 0.295 V, respectively, resulting in a ΔE_p value of 62 mV. The observed change in ΔE_p, which can be considered as one of the signatures of electrochemical reversibility, was not significant in this case. The electron transfer reactions on [i] GC and [ii] o-SWCNH/GC were studied at different scan rates over the range of 25–300 mV s^{-1}, and the respective peak parameters are listed in Table S1 (ESI†). The slopes of plots of $\ln(I_p^c)$ versus $\ln(\nu)$ on GC and o-SWCNH/GC were calculated as 0.48 (with R^2 = 0.9999) and 0.49 (with R^2 = 0.9926), respectively (Fig. S4[A], ESI†), where I_p^c represents the cathodic peak current. Therefore, it could be understood that the redox reaction of [Fe(CN)$_6$]$^{3-}$ on both electrodes happened through fast electron transfer reactions governed by the diffusion-controlled mass-transfer of analyte towards the electrode surface. Furthermore, it was understood that the nature of the oxygenated functional groups present on o-SWCNHs did not induce any additional electrostatic interactions with the negatively charged redox analytes ([Fe(CN)$_6$]$^{3-}$/[Fe(CN)$_6$]$^{4-}$) at pH 6.8. The electrochemically effective surface areas (A) of GC and o-SWCNH/GC were calculated to be 0.074 and 0.088 cm^2, respectively, through the Randles–Sevcik equation (eqn (2)) from plots of i_p^c versus $\nu^{\frac{1}{2}}$ (Fig. S4[B and C], ESI†):

$$i_p^c = 2.69 \times 10^5 n^{\frac{3}{2}} D^{\frac{1}{2}} A C \nu^{\frac{1}{2}} \qquad (2)$$

where, n, D and C are the stoichiometric electron transfer number per analyte molecule (here n = 1), the diffusion
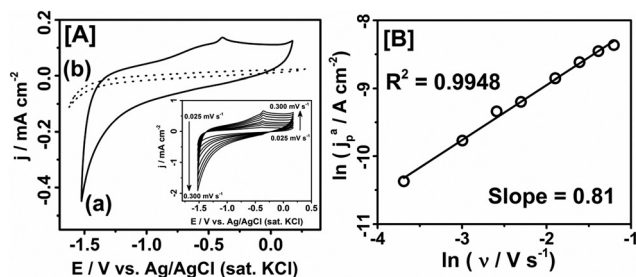
Fig. 3 [A] Cyclic voltammograms (CVs) of (a) o-SWCNH/GC and (b) bare GC in sat. Na$_2$CO$_3$ (pH 10.9) solution at ν = 25 mV s^{-1}; inset: CVs of o-SWCNH/GC in the same system at ν = 25, 50, 75, 100, 150, 200, 250 and 300 mV s^{-1}. [B] A plot of $\ln(I_p^a)$ versus $\ln(\nu)$ of o-SWCNH/GC.

coefficient of $[Fe(CN)_6]^{3-}$ ($D = 7.6 \times 10^{-6}$ cm^2 s^{-1})[68] and the concentration of $[Fe(CN)_6]^{3-}$ in the bulk solution (here $C = 5 \times 10^{-6}$ mol cm^{-3}), respectively. It can be seen from Fig. 4[A] that both electrodes showed comparable current densities (j) in CVs, although the ΔE_p value of o-SWCNH/GC was found to be slightly better than that of GC. Therefore, we studied the CVs further to calculate the standard heterogeneous electron transfer rate constant (k_0) for both electrodes. The rate and rate constant of the electron transfer reaction both increase on for an electrocatalysis reaction. The k_0 can be derived from the slope of the dimensionless current parameter Ψ (which defines the shape of the CV) with respect to $\left[\dfrac{n\pi FD\nu}{RT}\right]^{-\frac{1}{2}}$, as shown in eqn (3):

$$\Psi = \frac{k_0}{\left[\dfrac{n\pi FD\nu}{RT}\right]^{\frac{1}{2}}} \qquad (3)$$

where, F, R and T are the Faraday constant, universal gas constant and temperature on the absolute (Kelvin) scale, respectively. We developed an empirical formula (eqn (4)) to calculate Ψ from the experimentally observed ΔE_p values at different values of ν:[60]

$$\frac{1}{\Psi} = -2.11 + 34.67\Delta E_p - \frac{1}{2!} \times 39.56(\Delta E_p)^2 + \frac{1}{3!} \times 3570.42(\Delta E_p)^3 \qquad (4)$$

The k_0 values of the electron transfer reaction of $[Fe(CN)_6]^{3-}/$ $[Fe(CN)_6]^{4-}$ on GC and o-SWCNH/GC were calculated to be 8.58×10^{-3} and 5.59×10^{-2} cm s^{-1}, respectively, from the slopes of the plots of Ψ versus $\dfrac{1}{\left[\dfrac{n\pi FD\nu}{RT}\right]^{\frac{1}{2}}}$ (Fig. 4[B]). Therefore, it could be concluded that the rate of the electron transfer reaction of $[Fe(CN)_6]^{3-}/[Fe(CN)_6]^{4-}$ on o-SWCNH is catalyzed by the oxygenated functional groups of o-SWCNHs. However, we did not observe any electrostatic influence or overall improvement in the comparative current densities when using o-SWCNH/GC compared to a bare GC electrode. Fig. 4[C] shows the difference current density (j_d) values from the reduction of $[Fe(CN)_6]^{3-}$ in 0.1 M KCl on GC and o-SWCNH/GC. We should state here that j_d is the signal recorded by the instrument at each sampling potential after subtracting the current density sampled during the application of a reverse square-wave pulse from the current density sampled during the application of a forward square-wave pulse. The baseline current of the voltammogram corresponding to the o-SWCNH/GC electrode was found to be significantly negative, owing to pseudo-reactions of oxygenated functional groups of o-SWCNH. Thus, we calculated the peak current (j_d^p) of each voltammogram from the respective baseline current. j_d^p was calculated to be -7.7 and -9.9 mA cm^{-2} at 0.260 and 0.259 V for GC and o-SWCNH/GC, respectively. The electrocatalytic interaction of o-SWCNHs in the reduction of $[Fe(CN)_6]^{3-}$ could be understood from this result, and this was further supported by Nyquist plots of electrochemical

impedance spectroscopy carried out at 0.263 V with a sine potential perturbation with an amplitude of 5 mV in the linear frequency (f) range of 1×10^5 to 1×10^{-1} Hz (Fig. 4[D]). The impedance spectra were fitted with best possible physically realizable electrical equivalent circuits (EECs) (Fig. S5, ESI†), and the respective values of the circuit elements representing the solution resistance (R_s), charge transfer resistance (R_{CT}), constant phase element (CPE), Warburg impedance of semi-infinite diffusion (W), restricted diffusion (O), and resistance due to restricted diffusion (R_f) are listed in Table S2 (ESI†). R_s, R_{CT} and R_f represent the impedance responses from the orientation–reorientation of solvent molecules and ions from the supporting electrolyte at the interface, from the charge transfer reaction between the electrode and analyte, and from restricted diffusion of the analyte across the porous interface, respectively. The CPE is used to simulate/fit the impedance spectroscopy data, incorporating the energetic heterogeneity (i.e., the roughness) of the electrode surfaces. The CPE impedance is expressed via eqn (5):

$$Z_{CPE} = \frac{1}{Q_0[j\omega]^{n'}} \qquad (5)$$

where, Q_0, ω and n' are the frequency-independent parameter, the angular frequency ($\omega = 2\pi f$), and the parameter describing the deviation of the electrode–electrolyte interface from ideal capacitive behavior (i.e.; $n' = 1.0$, 0.0 and 0.5 represent pure resistive, pure capacitive and Warburg impedance behavior, respectively), respectively. Table S2 (ESI†) suggests that, although both electrodes deviate from ideal capacitive interface behavior due to the presence of energetically heterogeneous sites on the electrode surfaces, the presence of energetic heterogeneity is greater at o-SWCNH/GC compared to GC. The R_{CT} value for the $[Fe(CN)_6]^{3-}/$ $[Fe(CN)_6]^{4-}$ redox reaction decreased from 55.6 Ω on GC to 0.027 Ω on o-SWCNH/GC. In addition, with respect to the Randles EEC, the restricted diffusion of $[Fe(CN)_6]^{3-}/[Fe(CN)_6]^{4-}$ in the fine pores of o-SWCNH was responsible for the addition of R_f and O elements in the EECs for o-SWCNH/GC. The absence of any capacitive arc in the high-frequency region was confirmed from corresponding Bode plots (in terms of both the modulus impedance (Z) and phase angle (φ) versus $\log(f)$), as shown in Fig. S6 (ESI†).

A close inspection of Fig. 4[C](b) reveals an additional peak at -0.065 V, which results from other surface-bound reactions of o-SWCNHs. The currents sampled during the application of forward and reverse pulses in square wave voltammograms of $[Fe(CN)_6]^{3-}$ in 0.1 M KCl (pH 6.8) on GC and o-SWCNH/GC are shown in Fig. S7 (ESI†). The signature of surface-bound reactions of o-SWCNHs was evident from both forward and reverse currents at potentials of about -0.065 V. A shift in the potential of the surface-redox reactions of o-SWCNHs towards a less negative potential was evident in the presence of the $[Fe(CN)_6]^{3-}/[Fe(CN)_6]^{4-}$ redox reaction, but the actual reason for this is not known. Therefore, we chose $[Ru(NH_3)_6]^{3+}/$ $[Ru(NH_3)_6]^{2+}$ (formal redox potential, E_0', ~ -0.135 V) as a suitable redox reaction to study the interference from surface-bound reactions of o-SWCNHs on electron transfer reactions at nearby potentials.
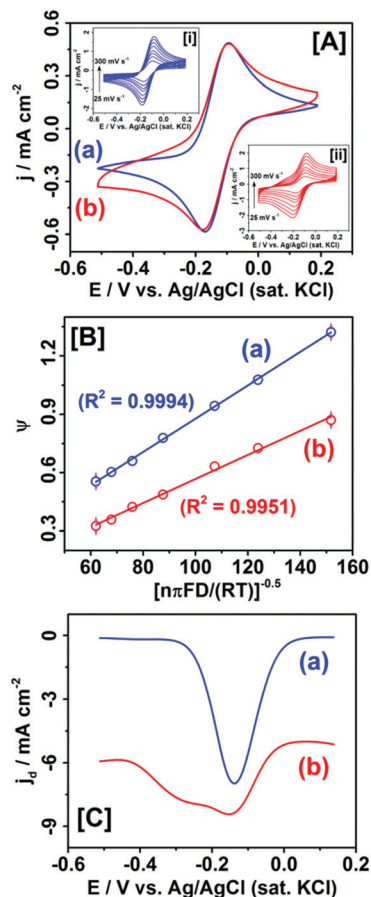
Fig. 5 [A] CVs of 5 mM [Ru(NH$_3$)$_6$]Cl$_3$ in 0.1 M KCl (pH 6.8) on (a) GC and (b) o-SWCNH/GC electrodes at ν = 25 mV s^{-1}; inset: CVs from the same system on [i] GC and [ii] o-SWCNH/GC at ν = 25, 50, 75, 100, 150, 200, 250 and 300 mV s^{-1}. [B] Plot of Ψ versus $\dfrac{1}{\left[\dfrac{n\pi FD\nu}{RT}\right]^{\frac{1}{2}}}$ from the same reaction on (a) GC and (b) o-SWCNH/GC. [C] The j_d values from cSWVs for the reduction of [Ru(NH$_3$)$_6$]$^{3+}$ in 0.1 M KCl on (a) GC and (b) o-SWCNH/GC. The square wave pulse amplitude and frequency were 0.05 V and 50 Hz, respectively.

Fig. 5[A] shows CVs from 5 mM [Ru(NH$_3$)$_6$]Cl$_3$ in 0.1 M KCl (pH 6.8) on GC and o-SWCNH/GC electrodes at ν = 25 mV s^{-1}. The E_p^c and E_p^a values of the [Ru(NH$_3$)$_6$]$^{3+}$/[Ru(NH$_3$)$_6$]$^{2+}$ redox reaction on bare GC were −0.170 and −0.095 V, respectively, resulting in a ΔE_p value of 75 mV. On the other hand, the E_p^c and E_p^a values of the same redox reaction on o-SWCNH/GC were −0.176 and −0.095 V, respectively, resulting in a ΔE_p value of 81 mV. The observed change in ΔE_p was not significant, but showed a different trend to our previous results from the [Fe(CN)$_6$]$^{3-}$/[Fe(CN)$_6$]$^{4-}$ redox reaction.

The electron transfer reactions on GC and o-SWCNH/GC were studied at different scan rates over the range of 25–300 mV s^{-1}, and the respective peak parameters are listed in Table S3 (ESI†). The slopes of plots of ln(I_p^c) versus ln(ν) on GC and o-SWCNH/GC were calculated to be 0.48 (with R^2 = 0.9999) and 0.49 (with R^2 = 0.9998), respectively (Fig. S8, ESI†). Therefore, it could be understood that the redox reaction of [Ru(NH$_3$)$_6$]$^{3+}$ on

both electrodes happened through fast electron transfer reactions governed by the diffusion-controlled mass transfer of analyte towards the electrode surface. Furthermore, it was understood that the nature of the oxygenated functional groups present on o-SWCNHs did not induce any additional electrostatic interactions with the positively charged redox analytes ([Ru(NH$_3$)$_6$]$^{3+}$/[Ru(NH$_3$)$_6$]$^{2+}$) at pH 6.8. The k_0 values of the electron transfer reactions of [Ru(NH$_3$)$_6$]$^{3+}$/[Ru(NH$_3$)$_6$]$^{2+}$ on GC and o-SWCNH/GC were calculated to be 8.6 × 10^{-3} and 6.2 × 10^{-3} cm s^{-1}, respectively, from the slopes of plots of Ψ versus $\dfrac{1}{\left[\dfrac{n\pi FD\nu}{RT}\right]^{\frac{1}{2}}}$ (Fig. 5[B]). Therefore, from similarities in the ΔE_p and k_0 values of the [Ru(NH$_3$)$_6$]$^{3+}$/[Ru(NH$_3$)$_6$]$^{2+}$ redox reaction on GC and o-SWCNH/GC electrodes, it could be concluded that the oxygen-functional groups of o-SWCNHs did not influence outer-sphere electron transfer from/to [Ru(NH$_3$)$_6$]$^{3+}$/[Ru(NH$_3$)$_6$]$^{2+}$, however, the proximity of the potentials of surface-bound redox reactions of o-SWCNHs to the redox reaction of [Ru(NH$_3$)$_6$]$^{3+}$/[Ru(NH$_3$)$_6$]$^{2+}$ sometimes distorted the voltammograms. Fig. 5[C] shows the difference current density (j_d) values from the reduction of [Ru(NH$_3$)$_6$]$^{3+}$ in 0.1 M KCl on GC and o-SWCNH/GC. Here also, the baseline current of the voltammogram corresponding to the o-SWCNH/GC electrode was found to be significantly negative owing to pseudo-reactions of the oxygenated functional groups of o-SWCNHs. Thus, we calculated the j_d^p value for each voltammogram from the respective baseline current. The j_d^p values were calculated to be −6.86 and −3.11 mA cm^{-2} at −0.138 and −0.153 V for GC and o-SWCNH/GC, respectively. In addition to that, an additional peak was observed at about −0.3 V for o-SWCNH/GC, and this was also evident in the current sampled during the application of forward and reverse pulses in the square wave voltammograms of [Ru(NH$_3$)$_6$]$^{3+}$ in 0.1 M KCl (pH 6.8) on GC and o-SWCNH/GC (Fig. S9, ESI†). Therefore, it was not the surface charge, but the surface-bound oxygenated functional groups of o-SWCNHs that could influence the kinetics of the inner-sphere heterogeneous electron transfer reactions of redox couples such as [Fe(CN)$_6$]$^{3-}$/[Fe(CN)$_6$]$^{4-}$ at positive potentials. o-SWCNHs did not influence the kinetics of outer-sphere heterogeneous electron transfer reactions of redox couples such as [Ru(NH$_3$)$_6$]$^{3+}$/[Ru(NH$_3$)$_6$]$^{2+}$ at negative potentials, and the close proximity of the redox potentials of the oxygenated functional groups of o-SWCNHs with the E_0' value of the [Ru(NH$_3$)$_6$]$^{3+}$/[Ru(NH$_3$)$_6$]$^{2+}$ redox couple prevented us from performing electrochemical impedance spectroscopy studies on this redox pair for further analysis.

On the basis of the above-mentioned results, we extended our studies to explore the electrochemical behavior of o-SWCNHs with respect to the quasi-reversible [U$^{(VI)}$O$_2$(CO$_3$)$_3$]$^{4-}$/[U$^{(V)}$O$_2$(CO$_3$)$_3$]$^{5-}$ redox couple ($E_0' \sim$ −0.75 V) in sat. Na$_2$CO$_3$ (pH 10.9). Fig. 6[A] shows the CVs of 0.8 mM [U$^{(VI)}$O$_2$(CO$_3$)$_3$]$^{4-}$ in sat. Na$_2$CO$_3$ (pH 10.9) on GC and o-SWCNH/GC at ν = 25 mV s^{-1}. The E_p^c and E_p^a values of [U$^{(VI)}$O$_2$(CO$_3$)$_3$]$^{4-}$ on GC were −1.265 and −0.218 V with j_p^c and j_p^a values of −0.188 and 0.104 mA cm^{-2}, respectively. The E_0' and ΔE_p values were calculated to be

−0.742 V[52] and 1.047 V, respectively. Therefore, a quasi-reversible electrochemical reaction involving the $[U^{(VI)}O_2(CO_3)_3]^{4-}/[U^{(V)}O_2(CO_3)_3]^{5-}$ redox couple on the GC electrode could be observed due to the stability of U(v) in sat. Na_2CO_3 (pH 10.9).[52,53] On the other hand, the E_p^c and E_p^a values of $[U^{(VI)}O_2(CO_3)_3]^{4-}$ on o-SWCNH/GC were −0.906 and −0.588 V, with j_p^c and j_p^a values of −0.258 and 0.230 mA cm^{-2}, respectively. The ΔE_p value of the reaction was decreased for o-SWCNH/GC compared to GC, to 0.318 V. The decreases in both the cathodic and anodic over-potentials by 0.359 V and 0.370 V, respectively, on o-SWCNH/GC compared to GC caused a significant decrease in the ΔE_p value of the reaction on o-SWCNH/GC by 0.729 V compared to GC. Hence, it can be concluded that the heterogeneous electron transfer kinetics of the $[U^{(VI)}O_2(CO_3)_3]^{4-}/[U^{(V)}O_2(CO_3)_3]^{5-}$ redox couple were significantly enhanced on o-SWCNHs compared to GC. Here, it should be declared that before planning and executing all the experiments, some preliminary electrochemical studies were performed with electrochemically reduced (at −1.6 V for 240 s in sat. Na_2CO_3 (pH 10.9)) o-SWCNH/GC with an electrochemically active surface area of 0.079 cm^2 (determined using the same procedure as followed for the other electrodes). Fig. S10 (ESI†) shows the CVs of 0.8 mM $[U^{(VI)}O_2(CO_3)_3]^{4-}$ in sat. Na_2CO_3 (pH 10.9) on o-SWCNH/GC and electrochemically reduced o-SWCNH/GC at ν = 25 mV s^{-1}. It can be clearly seen that the activity of the electrode became inferior following electrochemical reduction. The Nyquist plot (Fig. 6[B]) obtained at −0.742 V with a sine amplitude of 0.01 V over the frequency range of 1×10^5–0.02 Hz showed that the R_{CT} value of the $[U^{(VI)}O_2(CO_3)_3]^{4-}/[U^{(V)}O_2(CO_3)_3]^{5-}$ redox reaction

decreased from 181 kΩ (on GC) to 3.47 kΩ (on o-SWCNH/GC) at −0.742 V. The other electrochemical parameters obtained via fitting the experimentally obtained impedance data with the EEC (Fig. S5[A], ESI†) are shown in Table S4 (ESI†).

The corresponding Bode plots (in terms of both modulus impedance (Z) and phase angle (φ) versus log(f)) are shown in Fig. S11 (ESI†). o-SWCNH/GC showed a different relaxation process (with a φ_{max} value of −69.3° at 19.3 Hz) compared to GC (with a φ_{max} value of −77.6° at 560 Hz) during the electron transfer reactions of U(vi)/U(v) in sat. Na_2CO_3 (pH 10.9). The shift in the phase angle frequency of the reaction on o-SWCNH/GC compared to on bare GC is an indication that the electrochemical reaction occurred at o-SWCNHs and not at the bare GC electrode surface.[69] The exposure of the external oxygenated surfaces of o-SWCNHs and their structural defects, like horns, pentagons, etc., to the electrolyte may be responsible for the electrocatalysis of the U(vi)/U(v) reaction. Therefore, it can be understood that the oxygenated functional groups of o-SWCNHs significantly helped the interfacial electrochemistry of the $[U^{(VI)}O_2(CO_3)_3]^{4-}/[U^{(V)}O_2(CO_3)_3]^{5-}$ redox couple on o-SWCNH/GC. The CVs of 0.8 mM $[U^{(VI)}O_2(CO_3)_3]^{4-}$ in sat. Na_2CO_3 (pH 10.9) on GC and o-SWCNH/GC at ν = 25, 50, 75, 100, 150, 200, 250, and 300 mV s^{-1} are shown in Fig. 6. The peak parameters are shown in Table S5 (ESI†). It can be seen that the E_p^c and E_p^a values both symmetrically shift towards more negative and more positive potentials, respectively, by 163 mV upon increasing ν from 25 to 300 mV s^{-1}, but E_0' remains almost constant at −0.745 ± 0.003 V. The average absolute ratio of j_p^c/j_p^a was calculated to be 1.67, indicating a higher contribution from the cathodic reaction compared to the anodic reaction. The cathodic charge transfer coefficient (α_c), which is a representation of the fraction of the applied external potential that becomes effective for the electron transfer reaction, was calculated from eqn (6); the values were 0.25 ± 0.01 and 0.29 ± 0.03 for GC and o-SWCNH/GC electrodes, respectively, and these are found to be better than the value (0.111 ± 0.007) from the same system reported elsewhere.[53]

$$\alpha_c = \frac{0.04768}{E_{\frac{p}{2}}^c - E_p^c} \tag{6}$$

From the slopes of 0.49 ($R^2 = 0.9972$) and 0.45 ($R^2 = 0.9999$) of the plots of $\ln(j_p^a)$ versus $\ln(\nu)$ and $\ln(j_p^c)$ versus $\ln(\nu)$, respectively (inset of Fig. 6[C]), the reduction of $[U^{(VI)}O_2(CO_3)_3]^{4-}$ as well as the oxidation of $[U^{(V)}O_2(CO_3)_3]^{5-}$ on GC was found to be controlled by a diffusion-controlled mass transfer process. The diffusion coefficient of $[U^{(VI)}O_2(CO_3)_3]^{4-}$ in sat. Na_2CO_3 at room temperature (T = 298 K) was calculated to be 1.8×10^{-6} cm^2 s^{-1} from the slope of the plot of j_p^c versus $\nu^{\frac{1}{2}}$, using eqn (7).

$$i_p^c = 2.69 \times 10^5 n(n_a\alpha_c)^{\frac{1}{2}} D^{\frac{1}{2}} A C \nu^{\frac{1}{2}} \tag{7}$$

where n_a represents the number of electrons involved in the activation state (here we assume that n_a = 1 for the U(vi)/U(v) redox reaction). The calculated D value of $[U^{(VI)}O_2(CO_3)_3]^{4-}$ was found to be in the range of the reported values (3.73×10^{-6}) elsewhere.[53] The post-cathodic peak current for o-SWCNH/GC
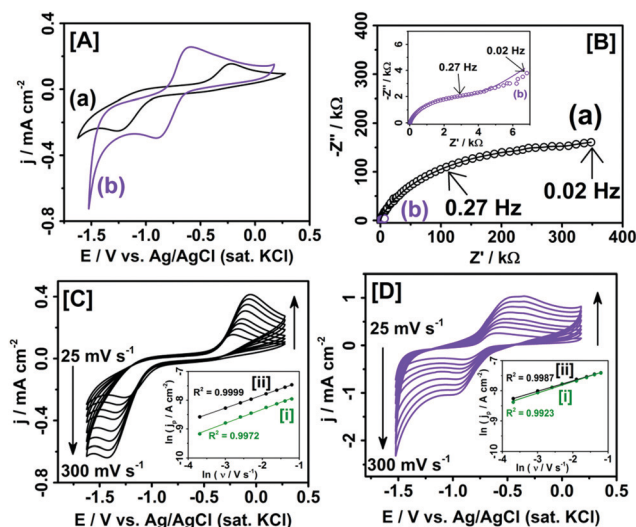

Fig. 6 [A] CVs of 0.8 mM $[U^{(VI)}O_2(CO_3)_3]^{4-}$ in sat. Na_2CO_3 (pH 10.9) on (a) GC and (b) o-SWCNH/GC at ν = 25 mV s^{-1}. [B] Nyquist plots of 0.8 mM $[U^{(VI)}O_2(CO_3)_3]^{4-}$ in sat. Na_2CO_3 (pH 10.9) on (a) GC and (b) o-SWCNH/GC at a fixed potential of −0.742 V with an amplitude of 0.01 V over the frequency range of 1×10^5–0.02 Hz. The solid lines show the calculated data obtained from fitting the impedance data with the Randles electrical equivalent circuit (Fig. S5[A], ESI†); inset: a magnified image showing the Nyquist plot for o-SWCNH/GC (b). CVs of 0.8 mM $[U^{(VI)}O_2(CO_3)_3]^{4-}$ in sat. Na_2CO_3 (pH 10.9) on [C] GC and [D] o-SWCNH/GC at ν = 25, 50, 75, 100, 150, 200, 250, and 300 mV s^{-1}; insets of [C] and [D]: plots of the respective [i] $\ln(j_p^a)$ versus $\ln(\nu)$ and [ii] $\ln(j_p^c)$ versus $\ln(\nu)$ values.

increased with increasing ν because of an increase in the rate of hydrogen evolution through the reduction of water (eqn (1)). Table S5 (ESI†) shows that the E_p^c and E_p^a values for o-SWCNH/GC both asymmetrically shifted towards more negative (by 144 mV) and positive (by 178 mV) potentials, respectively, upon increasing ν from 25 to 300 mV s^{-1}. Further, the average absolute ratio of j_p^c/j_p^a was calculated to be 1.04, indicating significant improvement in the oxidation of $[U^{(V)}O_2(CO_3)_3]^{5-}$ on o-SWCNH/GC compared to GC. Hence o-SWCNHs, which is p-type semiconducting material,[6] influence the quasi-reversible $[U^{(VI)}O_2(CO_3)_3]^{4-}/[U^{(V)}O_2(CO_3)_3]^{5-}$ redox reaction through the oxygenated functional groups. However, they did not change the overall mechanisms of the reduction of $[U^{(VI)}O_2(CO_3)_3]^{4-}$ and the oxidation of $[U^{(V)}O_2(CO_3)_3]^{5-}$ on o-SWCNH/GC, which are governed by diffusion-controlled mass transfer, as understood from the slopes of 0.38 ($R^2 = 0.9923$) and 0.35 ($R^2 = 0.9987$) of $\ln(j_p^a)$ *versus* $\ln(\nu)$ and $\ln(j_p^c)$ *versus* $\ln(\nu)$, respectively (inset of Fig. 6[D]). It should be mentioned that these values are found to be closer to an ideal value of 0.5 (for a diffusion-controlled reaction) than an ideal value of 1.0 (for an adsorption-controlled reaction) within the limits of the experimental conditions, and we suspect that interfering reactions involving the surface functionalities of o-SWCNH/GC influenced the baseline currents of the quasi-reversible electron transfer reactions and decreased the values of the slopes compared to GC. Furthermore, we are not in a position to completely exclude the effects of electrostatic repulsion between the negatively charged surfaces of o-SWCNHs at pH 10.9 and $[U^{(VI)}O_2(CO_3)_3]^{4-}/[U^{(V)}O_2(CO_3)_3]^{5-}$ ions on these peak currents.

Then, the k_0 values of the electrochemical reaction of the $[U^{(VI)}O_2(CO_3)_3]^{4-}/[U^{(V)}O_2(CO_3)_3]^{5-}$ redox couple in sat. Na$_2$CO$_3$ (pH 10.9) were calculated from the slopes of plots of Ψ *versus* $\dfrac{1}{\left[\dfrac{n\pi FD\nu}{RT}\right]^{\frac{1}{2}}}$ (Fig. 7[A]) to be $2.8 \pm 0.08 \times 10^{-6}$ ($R^2 = 0.9993$) and $1.1 \pm 0.03 \times 10^{-4}$ ($R^2 = 0.9991$) cm s^{-1} on GC and o-SWCNH/GC, respectively. Therefore, the higher k_0 value for the $[U^{(VI)}O_2(CO_3)_3]^{4-}/[U^{(V)}O_2(CO_3)_3]^{5-}$ redox reaction on o-SWCNH/GC compared to GC was the result of the inner-sphere electrocatalytic action of the oxygenated functional groups as well as the pentagonal structural defects of o-SWCNHs on electron transfer to and from $[U^{(VI)}O_2(CO_3)_3]^{4-}$ and $[U^{(V)}O_2(CO_3)_3]^{5-}$, respectively. The o-SWCNH/GC electrode showed a stable electrochemical CV signal from 0.8 mM $[U^{(VI)}O_2(CO_3)_3]^{4-}$ in sat. Na$_2$CO$_3$ for at least 15 continuous potential cycles at a scan rate of 50 mV s^{-1} (Fig. 7[B]). Also, Fig. 7[C] shows that o-SWCNH/GC modified electrodes were very reproducible, and four o-SWCNH/GC electrodes (named E1, E2, E3 and E4) prepared *via* similar procedures showed very similar CVs, except for the hydrogen evolution region, from 0.8 mM $[U^{(VI)}O_2(CO_3)_3]^{4-}$ in sat. Na$_2$CO$_3$ at a scan rate of 50 mV s^{-1}.

Therefore, the performance of o-SWCNH/GC was tested using blank subtracted cathodic square wave voltammograms (cSWVs) for the reduction of $[U^{(VI)}O_2(CO_3)_3]^{4-}$ with progressively increasing concentrations of U(VI) in the range of 70–681.5 µg L^{-1} in sat.
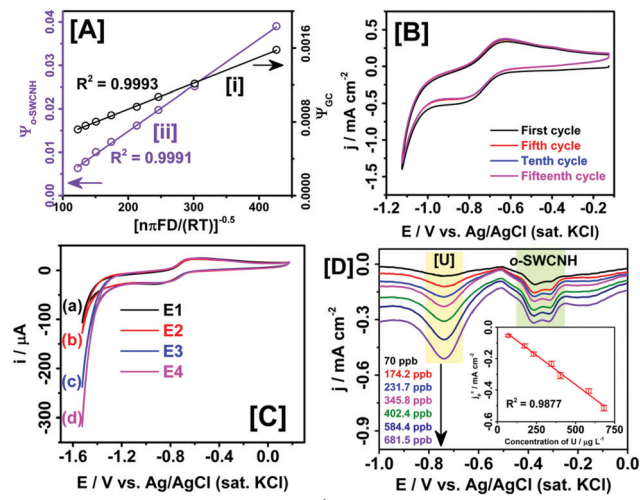

Fig. 7 [A] Plots of Ψ *versus* $\dfrac{1}{\left[\dfrac{n\pi FD\nu}{RT}\right]^{\frac{1}{2}}}$ for [i] GC and [ii] o-SWCNH electrodes calculated from the CVs of 0.8 mM $[U^{(VI)}O_2(CO_3)_3]^{4-}$ in sat. Na$_2$CO$_3$ (pH 10.9) at different scan rates. [B] CVs of 0.8 mM $[U^{(VI)}O_2(CO_3)_3]^{4-}$ in sat. Na$_2$CO$_3$ (pH 10.9) on o-SWCNH/GC from the first, fifth, tenth and fifteenth potential cycle at $\nu = 50$ mV s^{-1}. [C] CVs of 0.8 mM $[U^{(VI)}O_2(CO_3)_3]^{4-}$ in sat. Na$_2$CO$_3$ (pH 10.9) at $\nu = 50$ mV s^{-1} from four o-SWCNH/GC electrodes (*viz.* E1, E2, E3 and E4) prepared *via* similar procedures. [D] Blank subtracted cSWVs on o-SWCNH/GC in sat. Na$_2$CO$_3$ (pH 10.9) solution containing 70.0, 174.2, 231.7, 345.8, 402.4, 584.4 and 681.5 µg L^{-1} (or ppb) U(VI) at an amplitude and a frequency of 0.05 V and 50 Hz, respectively; inset of [D]: a calibration plot of the difference peak current density (j_d^p) from cSWV with respect to the concentration of U(VI) in ppb on o-SWCNH/GC. The standard deviation from eight repeatable measurements is plotted as an error bar for each signal.

Na$_2$CO$_3$ (Fig. 7[D]). The sensitivity of the cSWV measurements was calculated as 0.75 µA cm^{-2} (µg L^{-1})$^{-1}$ from a plot of the mean peak current densities along with the standard deviation from eight repetitive measurements for each concentration of U(VI), as shown in the inset of Fig. 7[D]. A reliable wide linear dynamic range was also shown. Furthermore, one doublet cathodic peak at about −0.350 V originated from differences in the peak potentials of the forward and backward peak currents involving pseudo-redox reactions of the oxygenated functional groups of o-SWCNH/GC (Fig. S12, ESI†), and its current also increased upon increasing the concentration of U(VI). Therefore, under the present experimental limitations, it could be ascertained that the oxygenated functional groups of o-SWCNHs played different roles in the electrocatalysis of three different redox reactions, *viz.* $[Fe(CN)_6]^{3-}/[Fe(CN)_6]^{4-}$ in 0.1 M KCl (pH 6.8); $[Ru(NH_3)_6]^{3+}/[Ru(NH_3)_6]^{2+}$ in 0.1 M KCl (pH 6.8) and $[U^{(VI)}O_2(CO_3)_3]^{4-}/[U^{(V)}O_2(CO_3)_3]^{5-}$ in sat. Na$_2$CO$_3$ (pH 10.9), over different electrochemical potential windows. The active sites of the oxygenated functional groups of o-SWCNHs could reduce the electron transfer barrier for the $[Fe(CN)_6]^{3-}/[Fe(CN)_6]^{4-}$ redox reaction; the concurrent redox reactions of the oxygenated functional groups interfered with the electrochemical signals of the $[Ru(NH_3)_6]^{3+}/[Ru(NH_3)_6]^{2+}$ redox reaction, but did not influence the outer-sphere electron transfer reactions; and, at higher negative potentials, the ionized carboxylate functional

groups of o-SWCNHs could mimic part of the complexing carbonate unit to uranyl carbonates and could mediate the inner-sphere redox reaction of $[U^{(VI)}O_2(CO_3)_3]^{4-}/[U^{(V)}O_2(CO_3)_3]^{5-}$.

4. Conclusions

The hidden potential of o-SWCNHs in heterogeneous catalytic electron transfer reactions involving inorganic redox couples could be revealed through the above results. In fact, it was evident that the oxygenated functional groups of o-SWCNHs could influence the inner-sphere electron transfer reactions. Furthermore, the electrocatalytic action and electroanalytical merits of o-SWCNHs in relation to the electrochemistry of the $[U^{(VI)}O_2(CO_3)_3]^{4-}/[U^{(V)}O_2(CO_3)_3]^{5-}$ redox reaction were found to be highly promising for further exploration. Since o-SWCNHs can be economically produced on a very large scale without using any metal catalysts, we hope that the results shown in this article may boost research into the development of highly stable metal-free carbon-based electrocatalysts for further potential applications.

Conflicts of interest

The authors declare no conflicts of interest.

Acknowledgements

References

1 N. Choudhary, S. Hwang and W. Choi, in *Handbook of Nanomaterials Properties*, ed. B. Bhushan, D. Luo, S. R. Schricker, W. Sigmund and S. Zauscher, Springer Berlin Heidelberg, Berlin, Heidelberg, 2014, pp. 709–769.
2 S. Iijima, *Nature*, 1991, **354**, 56.
3 S. Iijima and T. Ichihashi, *Nature*, 1993, **363**, 603.
4 S. Iijima, M. Yudasaka, R. Yamada, S. Bandow, K. Suenaga, F. Kokai and K. Takahashi, *Chem. Phys. Lett.*, 1999, **309**, 165–170.
5 R. Yuge, F. Nihey, K. Toyama and M. Yudasaka, *Carbon*, 2017, **122**, 665–668.
6 N. Karousis, I. Suarez-Martinez, C. P. Ewels and N. Tagmatarchis, *Chem. Rev.*, 2016, **116**, 4850–4883.
7 D. Kasuya, M. Yudasaka, K. Takahashi, F. Kokai and S. Iijima, *J. Phys. Chem. B*, 2002, **106**, 4947–4951.
8 H. Wang, M. Chhowalla, N. Sano, S. Jia and G. A. J. Amaratunga, *Nanotechnology*, 2004, **15**, 546.
9 T. Azami, D. Kasuya, R. Yuge, M. Yudasaka, S. Iijima, T. Yoshitake and Y. Kubo, *J. Phys. Chem. C*, 2008, **112**, 1330–1334.
10 T. Azami, D. Kasuya, T. Yoshitake, Y. Kubo, M. Yudasaka, T. Ichihashi and S. Iijima, *Carbon*, 2007, **45**, 1364–1367.
11 L. Hawelek, M. Schiavon, J. Szade, P. Wlodarczyk, K. Jurkiewicz, H. E. Fischer, A. Kolano-Burian and A. Burian, *Diamond Relat. Mater.*, 2017, **72**, 26–31.
12 D. Kumar, K. Avita, K. Singh, V. Verma and H. S. Bhatti, *Dig. J. Nanomater. Biostructures*, 2014, **9**, 1713–1727.
13 S. Zhu and G. Xu, *Nanoscale*, 2010, **2**, 2538–2549.
14 Y. Liu, C. M. Brown, D. A. Neumann, D. B. Geohegan, A. A. Puretzky, C. M. Rouleau, H. Hu, D. Styers-Barnett, P. O. Krasnov and B. I. Yakobson, *Carbon*, 2012, **50**, 4953–4964.
15 X. Wang, M. Lou, X. Yuan, W. Dong, C. Dong, H. Bi and F. Huang, *Carbon*, 2017, **118**, 511–516.
16 R. Yuge, T. Manako, K. Nakahara, M. Yasui, S. Iwasa and T. Yoshitake, *Carbon*, 2012, **50**, 5569–5573.
17 C.-M. Yang, Y.-J. Kim, M. Endo, H. Kanoh, M. Yudasaka, S. Iijima and K. Kaneko, *J. Am. Chem. Soc.*, 2007, **129**, 20–21.
18 A. Izadi-Najafabadi, T. Yamada, D. N. Futaba, M. Yudasaka, H. Takagi, H. Hatori, S. Iijima and K. Hata, *ACS Nano*, 2011, **5**, 811–819.
19 S. Deckers, J. Steverlynck, P. Willot, S. Vandendriessche, G. Koeckelberghs, I. Asselberghs, T. Verbiest and M. A. van der Veen, *J. Phys. Chem. C*, 2015, **119**, 18513–18517.
20 S. Maiti and B. B. Khatua, *eXPRESS Polym. Lett.*, 2014, **8**, 895–907.
21 G. Zhu, M. N. Fiston, J. Qian and O. J. Kingsford, *Anal. Methods*, 2019, **11**, 1125–1130.
22 O. J. Kingsford, J. Qian, D. Zhang and Y. Yi, *Anal. Methods*, 2018, **10**, 5372–5379.
23 Y. Yi, O. Jibrael, M. Nkulu, J. Qian, Z. Liu, L. Liu and G. Zhu, *J. Electroanal. Chem.*, 2017, **801**, 38–42.
24 H. M. T. Assumpç, F. C. Vicentini, G. Gabriel, D. Oliveira and B. C. Janegitz, *Electrochim. Acta*, 2019, **298**, 893–900.
25 G. Zhu, H. Sun, B. Zou, Z. Liu, N. Sun, Y. Yi and K. Wong, *Biosens. Bioelectron.*, 2018, **106**, 136–141.
26 G. Xu, L. Gong, H. Dai, X. Li, S. Zhang, S. Lu, Y. Lin, J. Chen, Y. Tong and G. Chen, *Anal. Methods*, 2013, **5**, 3328–3333.
27 H. Dai, L. Gong, G. Xu, S. Zhang, S. Lu, Y. Jiang, Y. Lin, L. Guo and G. Chen, *Electrochim. Acta*, 2013, **111**, 57–63.
28 I. Ojeda, B. Garcinuño, M. Moreno-Guzmán, A. González-Cortés, M. Yudasaka, S. Iijima, F. Langa, P. Yáñez-Sedeño and J. M. Pingarrón, *Anal. Chem.*, 2014, **86**, 7749–7756.
29 F. Valentini, E. Ciambella, A. Boaretto, G. Rizzitelli, M. Carbone, V. Conte, F. Cataldo, V. Russo, C. S. Casari, D. F. Chillura-Martino, E. Caponetti, M. Bonchio, F. Giacalone, Z. Syrgiannis and M. Prato, *Electroanalysis*, 2016, **28**, 2489–2499.
30 S. Zhao, L. Wang, T. Wang, Q. Han and S. Xu, *Appl. Surf. Sci.*, 2016, **369**, 36–42.
31 J. Chen, P. He, H. Bai, H. Lei, K. Liu, F. Dong and X. Zhang, *J. Electroanal. Chem.*, 2017, **784**, 41–46.
32 M. V. Bracamonte, M. Melchionna, A. Giuliani, L. Nasi, C. Tavagnacco, M. Prato and P. Fornasiero, *Sens. Actuators, B*, 2017, **239**, 923–932.
33 L. Yan, X. Niu, Z. Wen, X. Li, X. Li and W. Sun, *Int. J. Electrochem. Sci.*, 2016, **11**, 8972–8980.

34 J. Zhang, J. Lei, C. Xu, L. Ding and H. Ju, *Anal. Chem.*, 2010, **82**, 1117–1122.

35 X. Liu, H. Li, F. Wang, S. Zhu, Y. Wang and G. Xu, *Biosens. Bioelectron.*, 2010, **25**, 2194–2199.

36 S. Zhu, H. Li, W. Niu and G. Xu, *Biosens. Bioelectron.*, 2009, **25**, 940–943.

37 X. Liu, L. Shi, W. Niu, H. Li and G. Xu, *Biosens. Bioelectron.*, 2008, **23**, 1887–1890.

38 L. Brandão, M. Boaventura and P. Ribeirinha, *Int. J. Hydrogen Energy*, 2012, **37**, 19073–19081.

39 L. Zhang, N. Zheng, A. Gao, C. Zhu, Z. Wang, Y. Wang, Z. Shi and Y. Liu, *J. Power Sources*, 2012, **220**, 449–454.

40 M. Boaventura, L. Brandão and A. Mendes, *J. Electrochem. Soc.*, 2011, **158**, B394–B401.

41 C. Poonjarernsilp, N. Sano and H. Tamon, *Appl. Catal., B*, 2014, **147**, 726–732.

42 S. M. Unni, S. Ramadas, R. Illathvalappil, S. N. Bhange and S. Kurungot, *J. Mater. Chem. A*, 2015, **3**, 4361–4367.

43 C. Zhu, D. Liu, Z. Chen, L. Li and T. You, *J. Colloid Interface Sci.*, 2018, **511**, 77–83.

44 R. Yuge, N. Tamura, T. Manako, K. Nakano and K. Nakahara, *J. Power Sources*, 2014, **266**, 471–474.

45 S. Carli, L. Casarin, Z. Syrgiannis, R. Boaretto, E. Benazzi, S. Caramori, M. Prato and C. A. Bignozzi, *ACS Appl. Mater. Interfaces*, 2016, **8**, 14604–14612.

46 F. Lodermeyer, R. D. Costa, R. Casillas, F. T. U. Kohler, P. Wasserscheid, M. Prato and D. M. Guldi, *Energy Environ. Sci.*, 2015, **8**, 241–246.

47 F. Lodermeyer, R. D. Costa and D. M. Guldi, *ECS J. Solid State Sci. Technol.*, 2017, **6**, M3140–M3147.

48 B. Fresco-Cala, J. M. Jimenez-Soto, S. Cardenas and M. Valcarcel, *Microchim. Acta*, 2014, **181**, 1117–1124.

49 J. Wang, Z. Hu, J. Xu and Y. Zhao, *NPG Asia Mater.*, 2014, **6**, e84.

50 P. Chen and R. L. McCreery, *Anal. Chem.*, 1996, **68**, 3958–3965.

51 T. Doneux, A. de Ghellinck, E. Triffaux, N. Brouette, M. Sferrazza and C. Buess-Herman, *J. Phys. Chem. C*, 2016, **120**, 15915–15922.

52 S. K. Guin, A. S. Ambolikar and J. V. Kamat, *Electrochim. Acta*, 2015, **174**, 1002–1008.

53 A. Ikeda, C. Hennig, S. Tsushima, K. Takao, Y. Ikeda, A. C. Scheinost and G. Bernhard, *Inorg. Chem.*, 2007, **46**, 4212–4219.

54 Carbonium, Carbonium, srl, Italy, http://www.carbonium.it/public/site/index.php.

55 S. R. Sahu, V. R. Rikka, M. Jagannatham, P. Haridoss, A. Chatterjee, R. Gopalan and R. Prakash, *Mater. Res. Express*, 2017, **4**, 35008.

56 B. Fresco-Cala, Á. I. López-Lorente and S. Cárdenas, *Nanomaterials*, 2018, **8**, 370.

57 S. Bandow, F. Kokai, K. Takahashi, M. Yudasaka, L. C. Qin and S. Iijima, *Chem. Phys. Lett.*, 2000, **321**, 514–519.

58 Y. Saito, T. Yoshikawa, S. Bandow, M. Tomita and T. Hayashi, *Phys. Rev. B: Condens. Matter Mater. Phys.*, 1993, **48**, 1907–1909.

59 B. Li, Y. Nan, X. Zhao, X. Song, H. Li, J. Wu and L. Su, *Appl. Phys. Lett.*, 2017, **111**, 221905.

60 S. K. Guin, A. S. Ambolikar, J. P. Guin and S. Neogy, *Sens. Actuators, B*, 2018, **272**, 559–573.

61 K. Sasaki, Y. Sekine, K. Tateno and H. Gotoh, *Phys. Rev. Lett.*, 2013, **111**, 116801.

62 F. Valentini, E. Ciambella, V. Conte, L. Sabatini, N. Ditaranto, F. Cataldo, G. Palleschi, M. Bonchio, F. Giacalone, Z. Syrgiannis and M. Prato, *Biosens. Bioelectron.*, 2014, **59**, 94–98.

63 M. Gao, Y. Xu, X. Wang, Y. Sang and S. Wang, *Electroanalysis*, 2016, **28**, 1377–1382.

64 L. Chen, Y. Tang, K. Wang, C. Liu and S. Luo, *Electrochem. Commun.*, 2011, **13**, 133–137.

65 A. G. Krivenko, R. A. Manzhos and S. G. Protasova, *Electrochem. Commun.*, 2018, **96**, 57–60.

66 T. Kar, R. Devivaraprasad, R. K. Singh, B. Bera and M. Neergat, *RSC Adv.*, 2014, **4**, 57781–57790.

67 J. P. Guin, S. K. Guin, T. Debnath and H. N. Ghosh, *Carbon*, 2016, **109**, 517–528.

68 A. J. Bard and L. R. Faulkner, *Electrochemical Methods: Fundamentals and Applications*, Wiley, 2nd edn, 2006.

69 B. O. Agboola, S. L. Vilakazi and K. I. Ozoemena, *J. Solid State Electrochem.*, 2009, **13**, 1367–1379.